Design for 4D printing: A voxel-based modeling and simulation of smart materials

Germain Sossou, Frédéric Demoly, Hadrien Belkebir, H. Jerry Qi, Samuel Gomes, Ghislain Montavon

Version of Record: https://www.sciencedirect.com/science/article/pii/S0264127519302357
Manuscript_0e87bd2b9cdd07a23b02c7ae574246d5

Design for 4D printing: A voxel-based modeling and simulation of smart materials

Germain Sossou[1], Frédéric Demoly[1], Hadrien Belkebir[1], H. Jerry Qi[2], Samuel Gomes[1], Ghislain Montavon[1]

[1] ICB CNRS 6303, Univ. Bourgogne Franche-Comté, UTBM, 90010 Belfort, France
[2] G.W.W. School of Mechanical Engineering, Georgia Institute of Technology, Atlanta, GA 30332, USA

Abstract

In the wake of the breakthrough being by additive manufacturing (AM), there is another rapidly growing manufacturing progress: 4D printing (4DP). It is basically AM with, inter alia, smart materials (SMs). Owing to the stimulus-responsive behaviors of these materials, the parts so manufactured are imbued with the ability to change. 4DP is being given huge research efforts regarding its manufacturing aspects. However so little is made to let designers explore the so uncovered design space. Compared to DFAM, what could be called Design for 4D printing (DF4DP) does lag far behind. In this article, a modeling framework for simulating SMs and conventional materials behaviors on a voxel basis is proposed; this allows for arranging materials in any distribution and rapidly evaluating the behavior of the distribution. Homogeneous and heterogeneous objects made of conventional materials and SMs were modeled and simulated. The modeled SMs were limited to non-programmable shape changing SMs including: piezoelectric material, electro-/magneto-/photostrictive materials and hydrogel. A printed smart valve and a theoretical actuator (both from other publications) were used as test cases. These simulations have a speed reasonable for the design iterations needed in conceptual design phase and they yield results in good agreement with physics.

1. Introduction

Since its discovery in 1987 (under the stereolithography apparatus patent [1]) additive manufacturing has evolved from a prototyping process to a fully established manufacturing process. Mainly praised is its shape complexity characteristic, indeed thanks to this capability shapes that are infeasible with conventional (subtractive) manufacturing processes are now manufacturable. In addition to shape complexity, other characteristics are among the 3D printing revolution engines: hierarchical complexity (features size at almost any length scale can be realized within the same part), functional complexity (mechanisms – with sometimes embedded electronics – can be manufactured without any assembly operations), and material complexity (parts with any material distribution – MD – and properties are now feasible). This latter capability – such as reviewed in [2] – is best illustrated with the PolyJet [3] AM technique. This technique works by selectively depositing tiny droplets of UV curable resins, smoothing them in a thin layer and curing the layer, and by repeating this process in a layer-by-layer manner. Up to 3 base resins can be mixed into any ratio to generate materials with a large range of properties including color, transparency, shore hardness, and many others. The obtained mixtures are the so-called digital materials. Parts with almost any MD (and thus multiple properties) can then be printed. Fig.1 (a) shows an illustration of a multi-material part made by the PolyJet technique. The material complexity allowed by AM has been further demonstrated by Katsumi et al. [4] who developed a 3D printing machine for

depositing metal. Their machine has been used to print a functionally graded material whose properties range from a metal (with low meting temperature) to a polymer as shown in Fig.1 (b). As shown in [2] others AM techniques such as FDM or even SLA have been demonstrated to be able to print multi-material objects.

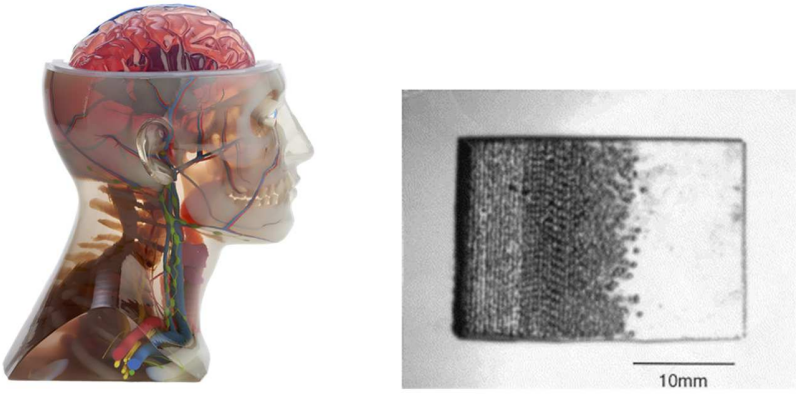

Fig.1 - Additive manufacturing's material complexity demonstrated by (a) a PolyJet printed model of human head [3], and (b) a functionally graded material made of metal and polymer [4]

In addition to the widely praised shape complexity allowed by AM, material complexity is expanding further the design space now available to designers, making creativity and imagination the main barriers. When the kinds of materials involved are taken into consideration the design freedom is more enlarged. Furthermore, the design space allowed by AM is being expanded further thanks to the interaction AM – smart materials (SMs), which has been coined as 4D Printing [5]. Here SMs are materials whose state changes upon exposure to a specific stimulus. These materials owe their smartness to both what they are sensitive to and how they respond to the stimuli. Examples include thermochromic materials [6], which change color under heat, magnetostrictive [7] materials which deform upon exposure to a magnetic field or electrorheological fluid [8] whose viscosity change with electricity. The characterization of their smartness can also be extended to whether their behaviors are reversible or not. The aforementioned material complexity of AM has been a main catalyst of what can be called the "4D revolution" making the AM-SMs interaction an attractive research topic. Indeed despite its infancy, many review papers have already been published on the topic [9-12]. The vast majority of current research work of 4DP is targeted at its manufacturing aspects (e.g. development of new materials [13], demonstration of new manufacturing routes for 4DP [14], etc.). However so little is made to make the so gained knowledge on 4DP available in a form usable by designers. In other words, compared to Design for Additive Manufacturing [15], what could be called Design for 4D printing (DF4DP) does lag far behind. A few works [16-19] have already attempted to fill that gap regarding shape memory polymers (SMP). These consist in constitutive modeling and development of bespoke finite element models for simulating the thermomechanical training of SMP and the subsequent shape recovery. What is sought through the use of SMs as raw materials in AM is basically to imbue structures with a smart behavior, in such a way that the material is/becomes the mechanism [20], and a passive source of energy (available in the environment or supplied internally) is what moves the mechanism to produce the desired/designed behavior. From a designer's point of view, questions that may then arise include: can one single SM be sufficient to produce a desired behavior? If no, what other materials should be combined to it? How can SMs be 'mixed' to produce a behavior? In a given spatial arrangement, how would a SM behave once subjected to the stimulus? Etc.

Answers to these questions require the capability to model and simulate the behaviors of SMs, especially in the conceptual design phase of the design process. It can be seen in the SMs-based actuators presented in [21] that the way SMs are spatially combined to another material in a part is key to how the part behaves upon exposure to the stimulus. Taken alone a SM would simply exhibit its basic behavior (whatever the size of the part made of it), however combined with a conventional material the resulting behavior may not be intuitive.

When designing for 4DP, there is therefore, inter alia, the need at some point to model and simulate the behavior of the considered SMs. Such modeling scheme should be at a granularity that allows for a seamless "intertwining" of SMs with other materials. Finally as designing the right distribution of SMs to achieve a desired functionality is not an intuitive task, the modeling scheme should also make design iteration easy and fast.

The objective of our work is to develop a voxel-based modeling framework that is intended to be used in the conceptual design phase. This voxel-based modeling framework is targeted at rapidly knowing how a MD would behave. As such the focus is on rapidly getting a qualitative answer to how a given distribution of SMs would behave. In this paper, which is the 1st part of a series of two, the framework for modeling and rapidly simulating the behavior of SMs is presented. In section 2, the foundations of our modeling scheme are established. Building on this, section 3 shows how SMs are modeled; a few simulations are run to validate the proposed framework in section 4. Finally conclusions are drawn and future work is stressed out.

2. Voxel mechanics modeling setup

As explained in the introduction section, regarding SMs, one MD generally equates to one concept. The explorative *3D painting* approach to determine a distribution – that is, the ability given to designers to pattern materials in any arrangement in order to test their distributions' behaviors – make it paramount to work on a framework which is fast (not too computationally costly). Moreover, this need for rapid iteration should not be at the cost of accuracy, even though the focus is mainly on a qualitative answer of how a given distribution would behave or what distribution would yield a prescribed behavior. For such modeling framework to be as physically realistic as possible and easily usable, it is required to:

- *Reproduce actual behavior of matter* – i.e. any deformation must be physically plausible and accurate.
- *Be volumetric*, as shape is involved – The actual three-dimensional shape of any modeled distribution should be reproduced.
- *Be sensitive* – Its behavior should be driven by changes in the environment. It must depend on variable measuring how much stimulus is sensed, so that behaviors are triggered accordingly.
- *Capture the actual behavior of the modeled SM* – Again, while the focus is not on accuracy, the proposed models for SMs should be based on declarative knowledge such as their existing constitutive equations.

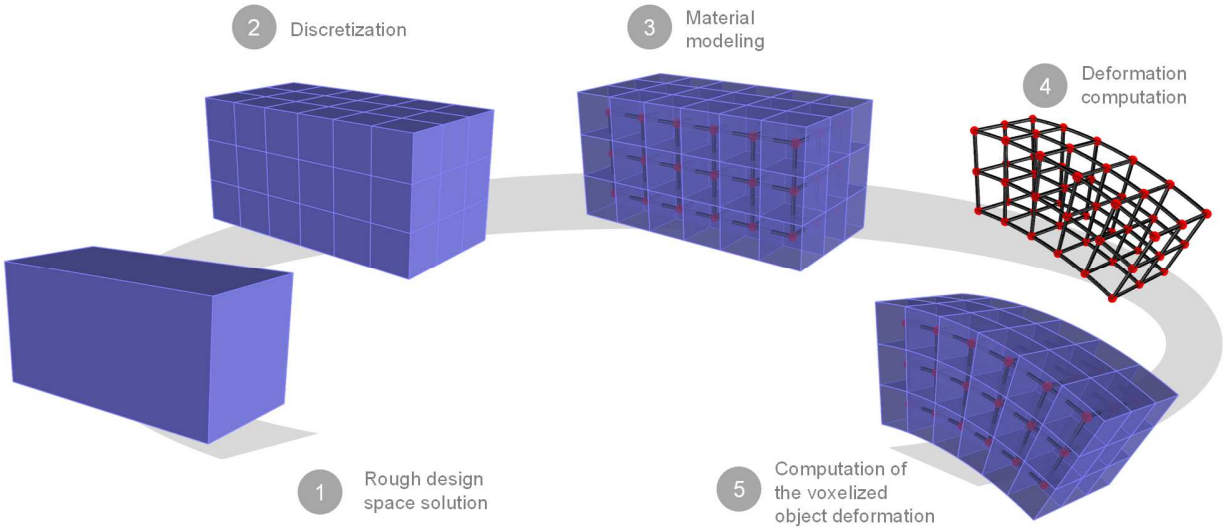

Fig. 2 – Continuum mechanics modeling setup

As shown in Fig. 2 the proposed approach for modeling conventional material behavior is organized in five main steps: (1) definition of rough design space, (2) discretization, (3) material modeling, (4) deformation computation and (5) computation of the voxelized object deformation. These steps are described in the following subsections. Such approach assumes that material properties in a single voxel are homogeneous, i.e. a voxel is made of a single homogeneous material.

The proposed methodology for computing the voxelized object deformation takes advantage of a well-established technique used in the computer graphics (CG) area: *skinning*; all the CG techniques bringing 3D characters to life fall under the umbrella of this term. Skinning [22] is the process of controlling deformations of a given object using a set of deformation primitives, which are transformations associated with bones of an animation skeleton. Roughly speaking, the overall skinning process can be described as: (1) skeleton extraction from the character geometry, the skeleton is then embedded within the geometry. A skeleton is composed of bones and joints. (2) Each vertex of the character is assigned a set of weights (each corresponding to a bone) quantizing how much that vertex is affected by transformations applied to the bones. (3) Applications of transformation (which are relative rotations) to the bones to animate the character.

2.1 Design space definition and discretization (Steps 1 and 2 of Fig. 2)

Here an approach similar to mass-spring modeling has been considered to simulate the mechanical behavior of matter. First of all, the geometry to be simulated is defined as the design space (step 1). Then the so defined shape is discretized – regardless of its (possible or intended) MD – into equally sized cubes: the voxels. Such representation and discretization of matter, despite being – depending of the chosen voxel size – at the cost of the accuracy of the represented geometry, allow for a finer control over the MD. In addition, chunking a shape into voxels does make the process of specifying a MD more intuitive compared to the use of spatial field functions [23] or others explicitly defined material functions [24]. As a shape is physically involved, spatial reasoning helps the cognitive aspect of the design process.

Voxels are connected (from their centers) not by springs but by three-dimensional beams. These beams form a 3D lattice frame, which acts as a backbone (or a control structure) of the whole shape. As they are

extending from center to center, the beams are then initially of a voxel size. The frame is what "holds" the matter together and that governs the deformation of the whole geometry.

2.2 Material modeling (Step 3 of Fig. 2)

Each voxel is assumed to be homogeneous and made of a single linear and isotropic material. Thus, the material properties required to fully characterize its mechanical behavior are limited to Young modulus (E) and shear modulus (G). As explained in section 3, for SMs, other material properties are added to account for their stimulus-responsive behavior.

As it is the frame deformation, which drives the object deformation, voxels' materials properties should be mapped to the beam material properties. To account for this, we have used an inheritance scheme: beams materials properties are inherited from the pairs of voxels they are connecting. In case where two voxels are made of the same material, the beam material properties are the same but when two voxels are of dissimilar materials, composite values for the material properties are taken for them, as described by the formulae:

$$E_c = \frac{2E_1E_2}{E_1 + E_2}, \qquad \text{and } G_c = \frac{2G_1G_2}{G_1 + G_2} \tag{1}$$

2.3 Deformation computation (Step 4 and Step 5 of Fig. 2)

Computation of the skeleton frame deformation (Step 4 of Fig. 2)

The beams forming the whole frame are modelled as 3D Euler-Bernoulli beams which resist axial, bending and twisting actions. Let *l* denote, the voxel size. The beam cross-section properties, assumed to be along the *X* axis, are as follows:

- Beam moments of inertia about the neutral (*x*) axis:

$$I_{yy} = I_{zz} = I = \frac{b \cdot h^3}{12} = \frac{l^4}{12} \tag{2}$$

- Beam moment of inertia characterizing torsional rigidity:

$$J_{xx} = J = \frac{bh(b^2 + h^2)}{12} = \frac{l^4}{6} \tag{3}$$

- Cross section area: $A = l^2$

The direct stiffness method [25] is used to compute the frame's degrees of freedoms (DOFs) and subsequently its deformed shape. Each node (again, which is a voxel's center) has six DOFs and the stiffness matrix for a beam oriented into the positive *x* direction is expressed (in its local coordinate system) as follows:

$$\overline{K_e} = \begin{pmatrix} R_a & 0 & 0 & 0 & 0 & 0 & -R_a & 0 & 0 & 0 & 0 & 0 \\ 0 & R_{z3} & 0 & 0 & 0 & R_{z2} & 0 & -R_{z3} & 0 & 0 & 0 & R_{z2} \\ 0 & 0 & R_{y3} & 0 & -R_{y2} & 0 & 0 & 0 & -R_{y3} & 0 & -R_{y2} & 0 \\ 0 & 0 & 0 & R_x & 0 & 0 & 0 & 0 & 0 & -R_x & 0 & 0 \\ 0 & 0 & -R_{y2} & 0 & 2 \cdot R_y & 0 & 0 & 0 & R_{y2} & 0 & R_y & 0 \\ 0 & R_{z2} & 0 & 0 & 0 & 2 \cdot R_z & 0 & -R_{z2} & 0 & 0 & 0 & R_z \\ -R_a & 0 & 0 & 0 & 0 & 0 & R_a & 0 & 0 & 0 & 0 & 0 \\ 0 & -R_{z3} & 0 & 0 & 0 & -R_{z2} & 0 & R_{z3} & 0 & 0 & 0 & -R_{z2} \\ 0 & 0 & -R_{y3} & 0 & R_{y2} & 0 & 0 & 0 & R_{y3} & 0 & R_{y2} & 0 \\ 0 & 0 & 0 & -R_x & 0 & 0 & 0 & 0 & 0 & R_x & 0 & 0 \\ 0 & 0 & -R_{y2} & 0 & R_y & 0 & 0 & 0 & R_{y2} & 0 & 2 \cdot R_y & 0 \\ 0 & R_{z2} & 0 & 0 & 0 & R_z & 0 & -R_{z2} & 0 & 0 & 0 & 2 \cdot R_z \end{pmatrix} \quad (4)$$

Where:

$$\begin{cases} R_a = \dfrac{EA}{L}, R_x = \dfrac{GJ}{L} \\ R_y = \dfrac{2EI_{yy}}{L}, \quad R_{y2} = \dfrac{6EI_{yy}}{L^2}, \quad R_{y3} = \dfrac{12EI_{yy}}{L^3} \\ R_z = \dfrac{2EI_{zz}}{L}, \quad R_{z2} = \dfrac{6EI_{zz}}{L^2}, \quad R_{z3} = \dfrac{12EI_{zz}}{L^3} \end{cases} \quad (5)$$

As the beams are located on a regular grid, each of them can be assumed to be oriented either into the positive x direction, y direction or z direction. The transformation matrix that is used to express their stiffness matrix in the global coordinate system (GCS) can therefore be easily pre-computed depending on their direction.

The nodes' DOFs, expressed in GCS, are represented by a vector:

$$U_i = [x_i \quad y_i \quad z_i \quad \theta_{xi} \quad \theta_{yi} \quad \theta_{zi}] \quad (6)$$

The whole system of equations is then formulated as:

$$KU = F \quad (7)$$

Where K is the global stiffness matrix, $U = [U_i \quad \dots \quad U_n]^T$ (n: number of voxels) and F a $6n$-vector containing the boundary conditions (including forces and moments and prescribed displacements and rotations). Once the DOFs are computed, they are used to compute the beam-deformed shape and ultimately the object deformed shape, as described in the following paragraph.

Computation of the voxelized object deformation (Step 5 of Fig. 2)

The voxelized object's deformation is controlled by the deformation of the beams. The idea of using a 3D lattice frame as a control structure of the whole shape is somewhat inspired by skeleton driven animation or more generally *skinning*, as introduced at the beginning of the section. The technique has been used as it is used by graphic designers (especially those involved in animation) except that the motion of the skeleton is physics-based (instead of user defined). Harnessing the relative simplicity of skinning to our voxel-based modeling and simulation approach is also a way of bridging the computational graphics, the computational mechanics and the manufacturing communities. Communities which may all have interests in 4DP.

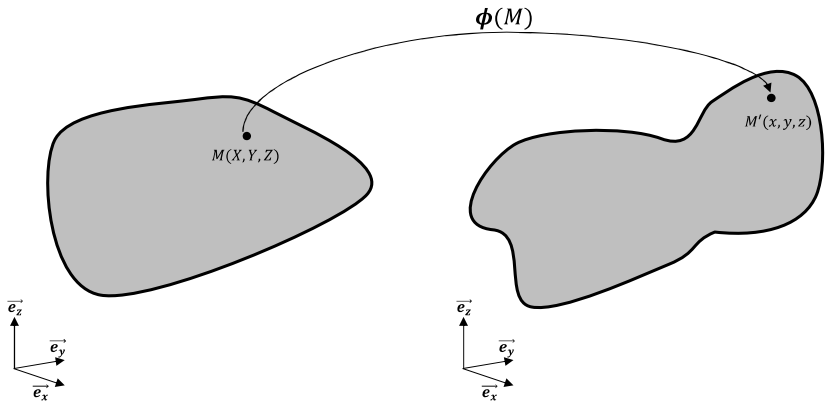

Fig. 3 - The deformation map

In our case, the frame acts as the skeleton and the DOFs of the nodes act as the transformations moving and deforming the beams (i.e. the bones). While, in the case of skinning, simple rotation matrices are enough to describe how the bones move, in our case there is the need to find a more complex mathematical representation of the bone motions. Indeed, these latter do not have only rigid body motion: they can translate, rotate, bend, shrink, twist, etc. It is known that the deformation of any deformable object can be described by a *deformation map*, that is, a function which maps any point of the object in its initial state, to the same material point in the deformed state, as illustrated in Fig. 3. This holds particularly for beams, when one needs to find its 3D deformed shape. With the deformation map associated to each beam, a step towards controlling the voxelized object's deformation with the frame's deformation can be achieved.

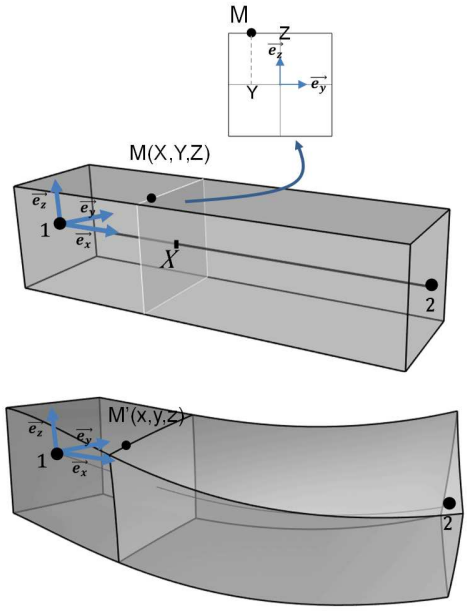

Fig. 4 - Beam's deformation map

We consider a beam oriented into the positive *x* direction as shown in ***Fig. 4***, with its centerline extending from node 1 to node 2. M(X,Y,Z) is an arbitrary point of the beam in the initial state. In the deformed

state, this point is located at M'(x,y,z). All the aforementioned coordinates are expressed in the beam local coordinate system as depicted in ***Fig. 4***. It can be shown [26] that:

$$M'(x,y,z) = \phi(M) = X\overrightarrow{e_x} + \begin{bmatrix} u_x(X) \\ u_y(X) \\ u_z(X) \end{bmatrix} + \Lambda(X) \begin{bmatrix} 0 \\ Y \\ Z \end{bmatrix} \tag{8}$$

Where $u_i(X)$ is the translational DOF along the i–axis at the position X. $\Lambda(X) = f\left(\theta_x(X), \theta_y(X), \theta_z(X)\right)$ (with $\theta_i(X)$ being the rotational DOF around the i–axis at the position X) is a tensor that characterizes the rotation in space of a cross section to which M belongs. More explicitly $\Lambda(X)$ is expressed as:

$$\Lambda(X) = R_z\big(\theta_z(X)\big) \cdot R_y\left(\theta_y(X)\right) \cdot R_x\big(\theta_x(X)\big) \tag{9}$$

Where R_i being the matrix of a rotation about the i–axis.

With the frame's deformation computation the values of the DOFs are only known at the nodes 1 and 2, so we used shape functions to extrapolate their values at any location along the beam (to reduce clutter the dependency on X has been omitted):

$$\begin{bmatrix} u_x \\ u_y \\ u_z \\ \theta_x \end{bmatrix} = \begin{bmatrix} N_1 & 0 & 0 & 0 & 0 & 0 & N_2 & 0 & 0 & 0 & 0 & 0 \\ 0 & N_3 & 0 & 0 & 0 & -N_4 & 0 & N_5 & 0 & 0 & 0 & -N_6 \\ 0 & 0 & N_3 & 0 & N_4 & 0 & 0 & 0 & N_5 & 0 & N_6 & 0 \\ 0 & 0 & 0 & N_1 & 0 & 0 & 0 & 0 & 0 & N_2 & 0 & 0 \end{bmatrix} U$$
$$\theta_y = -\frac{du_z}{dX}$$
$$\theta_z = \frac{du_y}{dX} \tag{10}$$

Where: $U = [u_{x1} \quad u_{y1} \quad u_{z1} \quad \theta_{x1} \quad \theta_{y1} \quad \theta_{z1} \quad u_{x2} \quad u_{y2} \quad u_{z2} \quad \theta_{x2} \quad \theta_{y2} \quad \theta_{z2}]^T$ and:

$$\begin{cases} N_1(X) = -\dfrac{1}{L}(X - X_2) \\ N_2(X) = \dfrac{1}{L}(X - X_1) \\ N_3(X) = 1 - \dfrac{3\bar{x}^2}{L^2} + \dfrac{2\bar{x}^3}{L^3} \\ N_4(X) = \bar{x}\left(-1 + \dfrac{2\bar{x}}{L} - \dfrac{\bar{x}^2}{L}\right), \quad \bar{x} = X - X_1 \\ N_5(X) = \dfrac{\bar{x}^2}{L^2}\left(3 - \dfrac{2\bar{x}}{L}\right) \\ N_6(X) = \dfrac{\bar{x}^2}{L}\left(1 - \dfrac{\bar{x}}{L}\right) \end{cases} \tag{11}$$

Equations (8-11) are all written in local coordinate system (LCS). On implementing them, they have been adapted to handle points coordinates in GCS and yield points in deformed state M' coordinates in GCS as well; an independence to the beam orientation has also been implemented. On a computational aspect,

morphing a parallelepiped beam according to the deformation of the underlying centerline was made by first meshing the beam surface and then moving the mesh's vertices by using the associated deformation map.

With each beam of the frame associated to a deformation map, there is one more step towards deforming the whole object. This is where skinning [22] has been harnessed to the proposed modeling framework. In our case, morphing the voxelized object according to the underlying skeleton frame is made through five steps:

1. **Voxel mesh's densification –** By default a voxel only has 8 vertices (its corners). Moving only these 8 vertices is not enough to accurately capture its actual deformed shape. That is why the number of vertices defining its shape must be increased by re-meshing its surface. The mesh density is therefore increased to 5-10 faces along each direction, which is high enough for an accurate mesh deformation.
2. **Extraction of the vertices set –** All the voxels' vertices are extracted and stored in a list without duplicates.
3. **Weights computations –** The vertices should move according to which beams they are (likely to be) influenced by. Therefore, we first define an influence zone for each beam, a zone which is the space occupied by the two voxels that the beam is connecting, any vertex belonging to this space is then influenced by the beam deformation. A vertex at the border between many influence zones is considered to belong to all these influence zones. Using these assumptions, all the beams influencing any vertex can be found. We consider each vertex to be equally influenced by its influencers, which yield the weights: $\omega_i = \frac{1}{N}$ for all the beams, where N is the number of beams influencing that vertex.
4. **Vertices motions –** Each vertex is then moved by using a weighted average deformation map (which is a blend of the influencing beams' deformation maps).
5. **Voxels shape update –** Finally each voxel shape is updated by using the new position of its vertices.

On a computational aspect, as moving any vertex is independent of the others locations, the process for deforming the voxelized object is friendly to parallelization, and hence speed.

2.4 Modeling scheme validation

2.4.1. Homogeneous structures simulations compared with Finite Element Analysis

While the proposed model of continuum mechanics modeling scheme is used as a tool for conceptual design (to rapidly know how a distribution qualitatively behaves), we found it worth gaging its accuracy compared to finite element method (FEM) simulations. Here two cases have been used to evaluate the modeling scheme:

- A cantilevered thick beam (50mm×10mm×10mm) made of a single material (E = 20GPa, G =7.69 GPa - structural steel) loaded at its free end with a 800N force.
- A thin squared plate (30mm×30mm×2mm) also made of a homogeneous MD (E=1000MPa, G=385MPa), fixed on the sides and loaded on a little square (3mm×3mm) at its center with a pressure of 16.5MPa.

For these two cases, the maximum displacement was used as a measure for comparison. For the beam a voxel size of 2mm was chosen, leading to a voxelized object of 25×5×5 voxels. The same voxel size was used for the plate which is then made of 15×15×2 voxels. The deformed shapes of the two cases are shown in ***Fig. 5***. The FEA was run using the commercial software Comsol Multiphysics®; free tetrahedral elements of the predefined size "fine" were used. The results of the simulation are outlined in Table 1.

Table 1 - Maximum displacement (mm) for the two cases

Case	**Proposed voxel-based model**	Finite Element Analysis
Beam	**1.86**	2.03
Thin plate	**3.7**	3.6

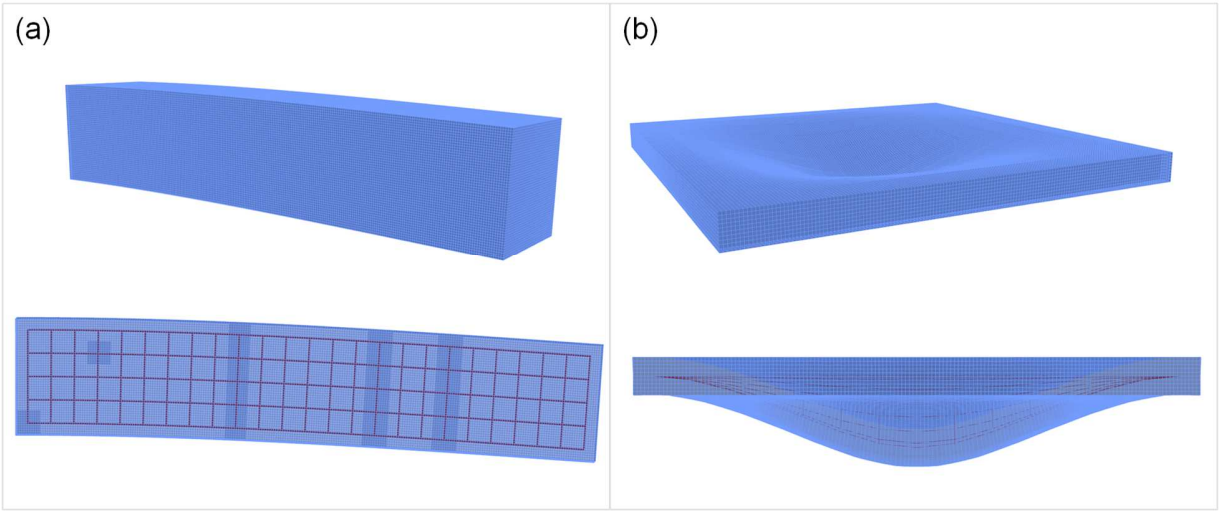

Fig. 5 - Two simulation cases with our modeling scheme: (a) cantilevered beam loaded at its free end, and (b) thin plate loaded fixed on the sides and at its center

For these two cases, the deformations are physically realistic and maximum displacements are within the ranges of the results obtained from finite element analysis (FEA) with an extremely fine mesh. This discrepancy from the results yielded by a FEA may have multiple causes. The two most plausible are: loads, boundary conditions (BCs) locations and voxel size (discretization) which are not independent. For the cantilevered beam case simulated in a FEA software, the force was applied as a force per unit area on the beam free end surface, and a fixed constraint (all DOFs set to zero) was set on the fixed end surface. In the proposed voxel-based modeling scheme, the force was equally distributed over the (25) voxels centers located at the free end, while the voxels centers located at the other end were fixed. The distance between where the beam is actually fixed and where the load is actually applied is shorter than in the real case simulated in the FEA software, therefore the beam actually simulated with our modeling scheme is stiffer than the actual one hence a lower maximum displacement. Furthermore, our modeling scheme does only support point loads (and moments) applied at the underlying frame's nodes; this is not the type of load which has been used in the FEA. Finally, as the voxel size decreases, BCs and loads get closer to their actual locations and their distributions get more accurate. In the beam case, we used a voxel size of 2mm which means BCs and loads locations are 1mm off their actual locations inwards the beam. Again, the proposed modeling scheme is not meant to be as accurate as established methods like FEM but is more aimed to provide qualitative evaluation of materials distributions in conceptual design.

2.4.2. **Qualitative evaluation for heterogeneous structures simulation**

The capability of our modeling scheme to handle multi-material simulation has also be somewhat gaged. We used a cantilevered beam with increasing stiffness along the width, the MD is such that five materials with Young moduli (all expressed in GPa) 0.08, 0.1, 0.8, 10 and 20 were arranged along the beam width as shown in Fig. ***6***.a. The beam is loaded at its free end with a 800N force. As one could expect stiffer sections would deform less since they are more load resistant; our model is able to reproduce this behavior as shown in Fig. 6.b.

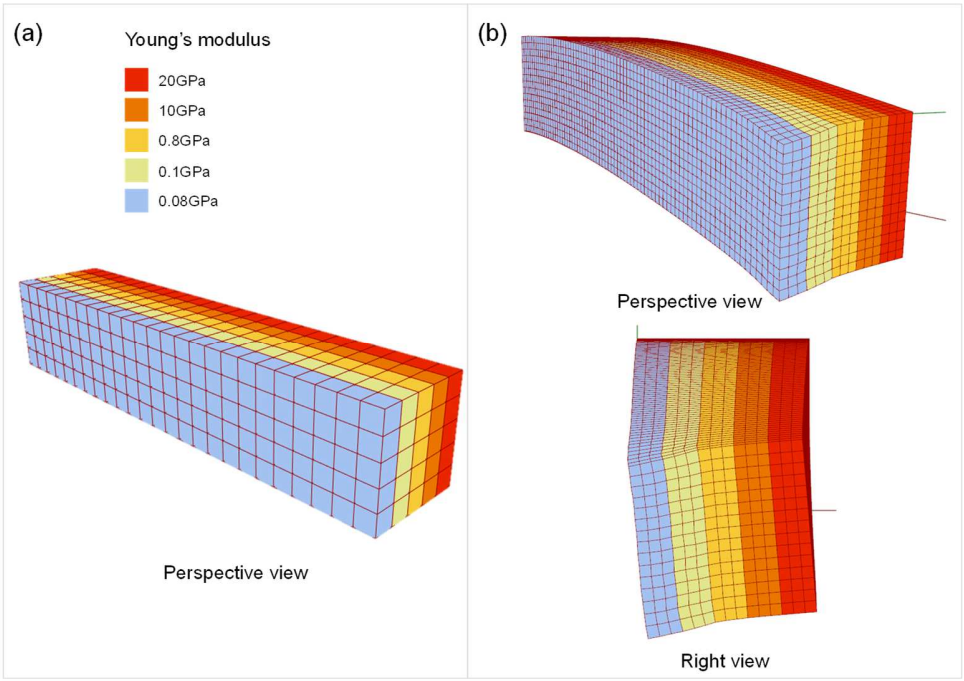

Fig. 6 – Multi-material beam with varying materials width wise

Another multi-material beam case has been simulated. We used a cantilevered beam with in the middle a material ways softer than the material of the remaining of the beam. A load oriented upwards was applied to its free end. As one could expect, the beam bends at the soft section (see Fig. 7).

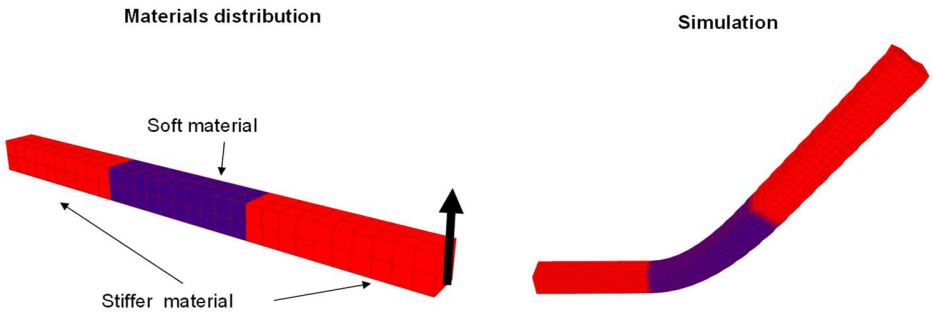

Fig. 7 - Cantilevered beam with a soft and hard materials distribution

3. Modeling the stimulus responsive behavior of smart materials

With the discovery of the shape memory effect and piezoelectricity, the range of SMs properties has significantly expanded, both in terms of stimuli and responses to these stimuli. While the main purpose of this section is not to provide a review of SMs, its endeavor to empower designers – which are likely to be non-experts of SMs – to use them, make it valuable to outline the SMs realm. Such a review would also direct how the stimulus responsive behaviors of these materials can realistically be modeled in the scheme we are using. Many SMs definitions exist in the literature, however all of them are in agreement with the fact that these are materials whose states are altered as a response to a specific change – a stimulus – in their environment. Behind such properties, can be seen the research endeavor to incorporate intelligence in the matter so that it behaves autonomously by sensing, reacting and adapting to the environment, as does any biological system.

Depending on how they respond to a stimulus, SMs may fall in any of the following groups:

- **Shape changers**: these are those which respond to stimuli by strain or stress. While some of them simply exhibit change in size (e.g. hydrogel, piezoelectric material, etc.) others, such as shape memory materials, react by changing shape.
- **Optical sensors:** within this group are materials whose response is optically perceivable; this includes for instance thermochromic materials, triboluminescent materials or switchable mirrors.
- **Converters:** these materials are those whose response is typically a signal that can be used as a stimulus for another SM or to provide information about a medium's state. Examples of such materials include piezoelectric material, thermoelectric material or photovoltaic material.
- **State changers:** SMs usually have a single condition; state changers are those whose conditions change in response to the right stimulus. Examples of these are electro-/magneto-rheological fluids or shear thickening fluids.

This categorization is the result of an analysis of the world of SMs as presented by Lefebvre, et al [27]. We consider as SMs, materials which sense and react to stimuli at their own, that is, which do not need another material to perform such functions. This excludes for instance dielectric elastomers [28], because even though they do shrink and expand in response to a potential difference, they are formed by the combination of the dielectric material sandwiched between two compliant electrodes. And the force causing this deformation is the electrostatic force attracting the electrodes together. In other words dielectric elastomers (sometimes referred to as electrostrictive materials) are not sensitive to an electric field without electrodes.

Our proposed approach has the potential to be used for a broad range of SMs; but for the purpose of illustrating the fundamental concept, we chose shape changers. The use of these latter to achieve a desired effect is quite challenging. Indeed as explained in the introduction, depending on how they are spatially arranged within a part, they can lead to totally different behaviors. Finding a right distribution to achieve a desired shape change is more challenging, for instance, than finding a distribution to achieve a visual effect. For some of the SMs which – in the current state of the art – work in liquid form and/or in homogeneous states, designing a MD might not be of interest. This is the case of converters and state changers. Therefore, as mentioned in the introduction, this paper is concerned with the shape changers group.

3.1 **Description of shape changing materials and materials' properties to be considered**

Within the group of shape changing materials (SCMs), it is worth distinguishing two subgroups [29]: *programmable* SCMs (p-SCMs) and *non-programmable* SCMs (np-SCM). In np-SCMs the way the material can change shape is predefined during fabrication and the shape change is limited to dimensions change (shrinking or expansion isotropically or not). p-SCMs change shape according to a pathway that can be altered regardless of how they were manufactured. In other words, after manufacturing they can be trained to shift shape between almost any shapes. These materials are typically shape memory materials [29, 30]. Basically, they are formed into one permanent shape, and can be thermo-mechanically trained (or *programmed*) to assume one (or several) temporary shape(s) from which the permanent shape can be recovered. As such achieving a specific shape change with p-SCMs is rather a thermomechanical training issue than a material spatial arrangement determination issue. That is why this work is focused on smart materials distribution with np-SCMs, which are described in the following paragraphs. The descriptions serve the purpose of briefly introducing the reader to them and most importantly they aim at deriving equations governing the materials' responses for our modeling scheme. First of all, we derive the stiffness equations for a generic member (or beam) made of a np-SCM.

For conventional (inert) materials, the beams' DOFs are governed by the member stiffness equations:

$$\bar{K}\bar{u} = \bar{f}_M \tag{12}$$

Where $\bar{f}_M$ is the vector containing all the (external) mechanical forces and moments applied to the beam (at its nodes). Equation (12) basically means that the only way for the beams to deform is by the mechanical forces and moment applied at their nodes. In our modelling scheme, the action of the smart materials will be modeled by introducing initial force effects, in a way similar to how thermal forces are modeled:

$$\bar{K}\bar{u} = \bar{f}_M + \bar{f}(\boldsymbol{S}) \tag{13}$$

$\boldsymbol{S}$ denotes the stimulus. For simplicity in understanding we will consider a planar bar member. In an unloaded state and upon exposure to the stimulus, its length is free to change from L to $L + \Delta L$, where ΔL is a function of the stimulus and the material properties:

$$\Delta L = L \times g(\boldsymbol{\alpha}, \boldsymbol{S}) \tag{14}$$

$\boldsymbol{\alpha}$ denotes a vector containing all the SMs properties related to its stimulus responsive behavior. The strain due to the stimulus can then be expressed as:

$$\epsilon_S = \frac{\Delta L}{L} = g(\boldsymbol{\alpha}, \boldsymbol{S}) \tag{15}$$

Now let's assume that the bar is also subjected to an (axial) force F causing the stress $\sigma = \frac{F}{A}$ (with A being the bar's cross-section), which induces the strain $\epsilon_M = \frac{\sigma}{E}$. The total strain in the bar is then:

$$\epsilon = \frac{\bar{u}_{x_j} - \bar{u}_{x_i}}{L} = \epsilon_M + \epsilon_S = \frac{\sigma}{E} + g(\boldsymbol{\alpha}, \boldsymbol{S}) \tag{16}$$

Which can be rewritten as follows:

$$\frac{EA}{L}\left(\bar{u}_{x_j} - \bar{u}_{x_i}\right) = \underbrace{\sigma A}_{\substack{mechanical \\ axial\ force}} + \underbrace{EAg(\boldsymbol{\alpha}, \boldsymbol{S})}_{\substack{internal\ force \\ induced\ by\ the\ stimulus}} = F \tag{17}$$

Where F denotes the total internal force. The joint forces are related to F as:

$$\begin{bmatrix} \bar{f}_{x_i} & \bar{f}_{y_i} & \bar{f}_{x_j} & \bar{f}_{y_j} \end{bmatrix} = \underbrace{\begin{bmatrix} \bar{f}_{Mx_i} & \bar{f}_{My_i} & \bar{f}_{Mx_j} & \bar{f}_{My_j} \end{bmatrix}}_{\bar{f}_M} + \underbrace{EAg(\boldsymbol{\alpha}, \boldsymbol{S}) \cdot \begin{bmatrix} -1 & 0 & 1 & 0 \end{bmatrix}}_{\bar{f}_S} \quad (18)$$

The member stiffness equations as:

$$\frac{EA}{L}\begin{bmatrix} 1 & 0 & -1 & 0 \\ 0 & 0 & 0 & 0 \\ -1 & 0 & 1 & 0 \\ 0 & 0 & 0 & 0 \end{bmatrix}\begin{bmatrix} \bar{u}_{x_i} \\ \bar{u}_{y_i} \\ \bar{u}_{x_j} \\ \bar{u}_{y_j} \end{bmatrix} = \bar{f}_M + \bar{f}_S \quad (19)$$

Regarding the beam elements used in our modeling scheme, the internal force due to the stimulus will be expressed as:

$$\bar{f}_S = EAg(\boldsymbol{\alpha}, \boldsymbol{S})[-1 \quad 0 \quad 0 \quad 0 \quad 0 \quad 0 \quad 1 \quad 0 \quad 0 \quad 0 \quad 0 \quad 0]^T \quad (20)$$

What will differentiate the various modeled SMs will be the expression of $g(\boldsymbol{\alpha}, \boldsymbol{S})$ and the conditions of application of the related force.

Piezoelectric material

Of interest in the scope of this paper is the reverse piezoelectric effect by which a voltage (or equivalently an electric field) generates strain. An inherent electrical property of these materials is what is called the polling direction, usually referred to as the 3-direction; it is the direction along which most of the electric dipoles within the material are oriented. The other two orthogonal directions are denoted 1 and 2. At constant stress, strain generated by an electric field is defined by the equation [31]:

$$\epsilon_j = d_{ij} E_i \quad (21)$$

Where:

- E_i, is the electric field in direction $i \in [\![1,3]\!]$;
- ϵ_j, is the generated strain in direction $j \in [\![1,6]\!]$, with the convention 4: 1-2, 5: 1-3, 6: 2-3 for the shear strains;
- d_{ij}, are piezoelectric strain coefficients.

Commonly used piezoelectric coefficients for actuation are d_{33} (strain along the polling direction induced by an electric field along that same direction) and d_{31}(strain along directions perpendicular to the polling direction by electric field's component along that same direction). Function $g(\boldsymbol{\alpha}, \boldsymbol{S})$ as introduced in equation 14 is then expressed as:

$$g(\boldsymbol{\alpha}, \boldsymbol{S}) = d_{3j} E_3 \quad (22)$$

In our modelling scheme piezoelectric material properties will be represented by the coefficients d_{33} and d_{31},they will also be characterized by a polling direction (*x*, *y* or *z*). The internal force due to the stimulus will depend on the beams orientation: for beams along E_3, d_{33}will be used for beams in perpendicular directions d_{31} will be used. This setup assumes then that only situations where the electric field is along the material polling direction can be simulated. The highest strains are in fact obtained in this situation.

Electrostrictive material

Dielectric materials are materials that do not conduct electricity, nevertheless they are responsive to electric field by (among others) exhibiting *electrostriction*. These materials are made of electric domains which are randomly oriented within the material. When a sample is subjected to an electric field, the electric domains get polarized along the electric field. As the opposite sides of these domains are then charged with opposite charges they attract each other, thus they shrink in the field direction and the elongate in perpendicular directions according to the material Poisson's ratio. The effect is a second order one, that is, the resulting deformation is proportional to the square of the electric field; particularly reversing the field does not change the sign of the strain. The so described mechanism is to be distinguished from what is usually referred to as electrostriction in dielectric polymers [28] and which is discarded from the scope of this work as explained in section 3 introduction.

In a stress free sample of the material, three electrostriction coefficients [32] can be defined to relate the induced deformations to the polarization:

$$\begin{bmatrix}\epsilon_1\\ \epsilon_2\\ \epsilon_3\\ \epsilon_4\\ \epsilon_5\\ \epsilon_6\end{bmatrix} = \begin{bmatrix}Q_{11} & Q_{12} & Q_{12} & 0 & 0 & 0\\ Q_{12} & Q_{11} & Q_{12} & 0 & 0 & 0\\ Q_{12} & Q_{12} & Q_{11} & 0 & 0 & 0\\ 0 & 0 & 0 & Q_{44} & 0 & 0\\ 0 & 0 & 0 & 0 & Q_{44} & 0\\ 0 & 0 & 0 & 0 & 0 & Q_{44}\end{bmatrix}\begin{bmatrix}P_1^2\\ P_1^2\\ P_1^2\\ P_2P_3\\ P_3P_1\\ P_1P_2\end{bmatrix} \tag{23}$$

Where $P = [P_1 \;\; P_2 \;\; P_3]$is the polarization vector. In case of induced polarization (which is the case when the material is subjected to an electric field), there is a single polarization direction, the one in the direction of the applied field. This direction is denoted 1, which zeros P_2 and P_3 from equation 23. The polarization is related to the electric field by: $P_1 = \epsilon E_1$, where ϵ is the static dielectric constant of the material. Equation 23 can then be rewritten as:

$$\begin{cases}\epsilon_1 = Q_{11}\epsilon^2 E_1^2 = M_{11}E_1^2\\ \epsilon_2 = Q_{12}\epsilon^2 E_1^2 = M_{12}E_1^2\\ \epsilon_3 = Q_{12}\epsilon^2 E_1^2 = M_{12}E_1^2\end{cases} \tag{24}$$

Function $g(\boldsymbol{\alpha}, \boldsymbol{S})$ will then be written as:

$$g(\boldsymbol{\alpha}, \boldsymbol{S}) = M_{1j}E_1^2 \tag{25}$$

Electrostrictive materials properties will then be represented by the coefficients M_{11} and M_{12}. The material polarization direction will be defined as the applied field's direction E_1. For beams along E_1, M_{11} will be used and for those in transverse directions M_{12} will be used.

Magnetostrictive materials

Any ferromagnetic (e.g. nickel, iron etc.), ferrimagnetic (e.g. iron II,III oxide) and antiferromagnetic (e.g. chromium, nickel oxide, etc.) material exhibits a phenomenon called magnetostriction. Once subjected to a magnetic field they exhibit a slight change in dimension. Roughly speaking this is due to rotation of magnetic dipoles within the material as they align with the applied magnetic field. There is a positive magnetostriction where the material elongates along the applied field, and a negative magnetostriction in which the material shrinks. For instance when exposed to a strong magnetic field iron can elongate by 0.002 %, while nickel contracts by 0.007%. Some of these materials are termed as "giant magnetostrictive materials" in reference to the higher strains they can produce. This is the case of Terfenol-D (up to 0.1%) or NiMnGa alloys (up to 9%). There are also dimensions' changes in the directions perpendicular to the

applied field. The effect is measured by the developed strain: $\lambda = \frac{\Delta L}{L} = f(H)$. H being the applied magnetic field. Similarly to electrostriction, it is a second order effect: reversing the applied magnetic field doesn't change the developed strain. Magnetostrictive materials are usually characterized [7] by their strain at magnetization saturation λ_s (which is the maximum strain – or minimum strain in case of negative magnetostriction – that can be developed by the material) and the saturation magnetic field H_s. In the region before saturation, the dependency of λ to H is quadratic.

In our modeling scheme, we will only consider the strain developed along the applied field (as it is the most significant) and values of magnetic field will be considered to be within the linear region before saturation. The material's magnetostrictive properties will be λ_s and H_s. Relation between magnetostriction and magnetic field can then be approximated by a linear law:

$$g(\boldsymbol{\alpha}, \boldsymbol{S}) = \lambda = \begin{cases} \frac{\lambda_s}{H_s}|H|, & |H| < H_s \\ \lambda_s, & |H| \geq H_s \end{cases} \tag{26}$$

Only beams along the applied field will be subjected to the internal force resulting from magnetostriction.

Photostrictive materials

Photostrictive materials are materials whose dimensions change when exposed to light, a change which is different from and more important than the one associated with heat induced by the light. Photostriction is found in four main types of materials [33] including ferroelectric materials, polar and non-polar semiconductors, and organic polymers. Some photostrictive materials shrink while others expand. The mechanism responsible of the phenomenon is quite different depending on the material: in ferroelectric material photostriction is due to a combination of photovoltaic and the reverse piezoelectric effect, whereas in organic polymers the phenomenon is due to photoisomerization (light induced change in molecule structure). The effect is usually quantified with a single measure of strain, usually denoted $\frac{\Delta L}{L}$ and referred to as photostriction coefficient, which is an indication that the behavior is isotropic. While in ferroelectric, photostriction coefficient of 0.45% is deemed as a giant photostrictive response, in nematic elastomers photostriction can be up to 400% [34]. The literature on these materials is populated with experimental data showing the developed strain versus light's wavelength [33], exposure time to light [34] and light's intensity [35] but there are no close form relationships between the electrostriction coefficient and these characteristics of the stimulus. In addition there is a dependence on light penetration depth. In our modeling scheme we elected to restrain the dependency of photostriction to light's intensity (as the easiest controllable parameter), the effect is modeled as:

$$\frac{\Delta L}{L} = kI \tag{27}$$

Where, I is light's intensity and k, a material property. This relationship is based on the experimental work reported in [35] (especially Figure 2.c of this paper). In addition a parameter for light penetration depth is introduced, this will tell the number of voxels (thus the number of beams) in the material thickness that are reached by light.

Hydrogel

Hydrogels – which only work in wet conditions – are able to absorb or repel water (in a way similar to a sponge, except that they can retain the absorbed water in such a way that even pressure on it, may not release the water), and thus they can drastically change volume. Depending on their chemical composition they can be responsive to heat (as in most encountered hydrogels), light, electricity, solution properties (pH, salinity, concentration of a specific constituent, etc.). The exhibited shape change is an isotropic either shrinkage or expansion, depending on the chemical composition. In the case of heat as stimulus, there is lower threshold by which the dimension's change begins (usually referred to as lower critical solution temperature – LCST). Away from the critical temperature, the change stops, as the material reaches an equilibrium state. The material behavior is usually tracked by a volumetric swelling ratio (VSR), whose definition varies according to authors. In [21], the following definition of VSR was used:

$$\nu_s = \frac{V_0}{V_s} \tag{28}$$

Where V_0 is the material's volume in dry state, and V_s the current material's volume in swollen state. As such: $0 < \nu_s \leq 1$. With this definition, the higher is ν_s , the lower is the material's volume. In the case of shrinkage of the material with rising temperature, VSR's dependency on temperature is expressed [21] as:

$$\nu_s(T) = \nu_s^{min} + \left(\nu_s^{max} - \nu_s^{min}\right)\left[1 + \exp\left(\frac{LCST - T}{k}\right)\right]^{-1} \tag{29}$$

Where T is the temperature, k is a constant controlling how gradual the transitional behavior around the LCST is, ν_s^{min} and ν_s^{max} are the limits of the swelling ratio in fully swollen and collapsed (dry) state respectively. As the dimension change is isotropic (strain resulting from the volume change is the same in all the directions), function $g(\boldsymbol{\alpha}, \boldsymbol{S})$ can be expressed as:

$$g(\boldsymbol{\alpha}, \boldsymbol{S}) = \left[\nu_s(T)\right]^{-\frac{1}{3}} - 1 \tag{30}$$

Any beam in our modeling scheme made of hydrogel will then be subjected to the internal force resulting from temperature-driven volume change.

3.2 **Stimulus modeling**

The stimuli triggering the aforementioned SMs are: heat, light, electric field or equivalently voltage, and magnetic field. These can clearly be separated in scalar stimuli and vector stimuli. In our modeling scheme a stimulus is considered as an environment variable that is sensed by each voxel (and thus each beam) the same way, that is, the value of the stimulus is considered to be the same for all the voxels. While such assumption is valid for electric or magnetic field (considering no electromagnetic shield is to be modeled), for heat and light it is questionable. Indeed heat propagates (from hot regions to colder ones) and light gets absorbed as it propagates through a medium. As the proposed modeling scheme is meant to be used in conceptual design (where the focus is more on functionality than accuracy), we elected not to take these phenomena into account. Nevertheless the framework may be extended to model all the stimuli field in the simulated object more accurately.

4. Validation with predefined distributions

In order to ascertain the accuracy of the proposed modeling framework for SMs modeling, a few existing MDs have been simulated. Namely the printed smart valve from [36] and the hypothetical actuators from [21]. All these examples are based on heat responsive hydrogel.

4.1 Smart hydrogel valve

Bakarich et al. [36] have demonstrated 4D printing with a smart valve. Basically the printed valve is able to regulate water flow according to this latter's temperature. The SM responsible of this behavior is a thermally responsive poly (N-isopropylacrylamide) hydrogel commonly referred to as PNIPAAm. Its LCST (cf. subsection 3.2.1) is between 32°C and 35°C. The material exhibits a large decrease in water content as the temperature is around LCST. The valve, as depicted in Fig. 8, has been printed with 2 materials: an epoxy based adhesive (Emax 904 Gel-SC) for the inert sections and hydrogel for the active sections. As water flows through the central tubing (from the top) and warms the actuating hydrogel strips, these shrink to close the outlet, thus blocking the water flow.

Materials' properties were used as measured in [36, 37] and are summarized in Table 2.

Table 2 - Material properties used for the smart valve

	E (MPa)	G (MPa)	ν_s^{min}	ν_s^{max}	LCST (°C)
Emax	2.7	0.96			
Hydrogel	1	0.35	0.98	0.4	33.5

The valve has been modeled with a voxel's size of 1mm. Voxels in the first row from the top were all fixed. Results of the simulation for an increasing temperature are shown in Fig. 8.

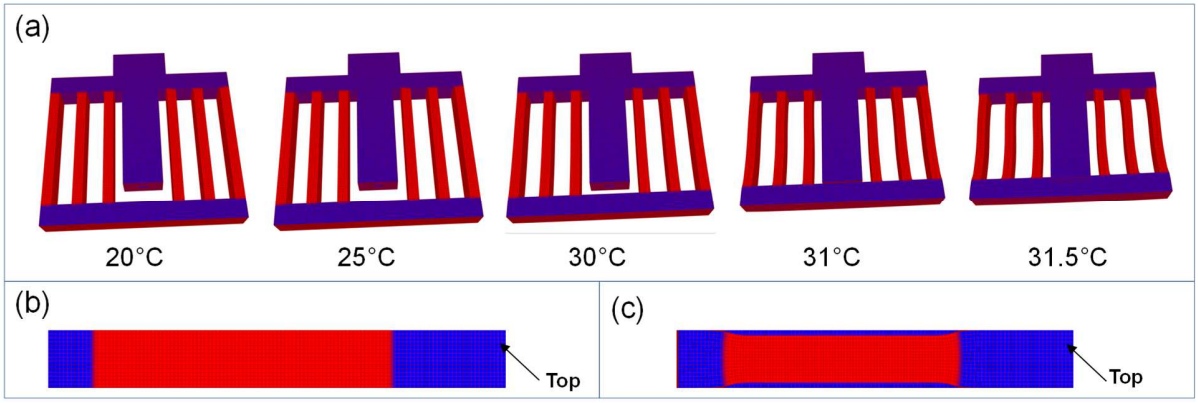

Fig. 8 – (a) Results of the simulation of the smart valve at various temperature – (b) Side view at 20°C – (c) Side view at 31.5°C

The shape change pattern yielded by our model is quite similar to the one exhibited by the actual printed valve as shown in [36]. The hydrogel strips clearly shrinks isotropically and pull the bottom inert section towards the tubing outlet.

4.2 **Hydrogel actuator**

In the previous example, the hydrogel sections work mostly in homogeneous configurations (the strips) and as such the motion they are responsible of are limited to one dimensional motions. This is a typical case in hydrogel applications. Using FEM based simulations Westbrook and Qi [21] designed hydrogel actuators that leverage heterogeneities to more complex shape changes. One of their theoretical actuators has (partially) been modeled and simulated with our voxel-based framework. It is the in which hydrogel shrinking is converted into bending. Such motion has been realized by patterning the hydrogel (red) into another non responsive hydrogel (blue) as shown in Fig. 9. Materials' properties were used from their study (some of them were estimated). The simulated actuator is simulated with the left end (see Fig. 9) fixed.

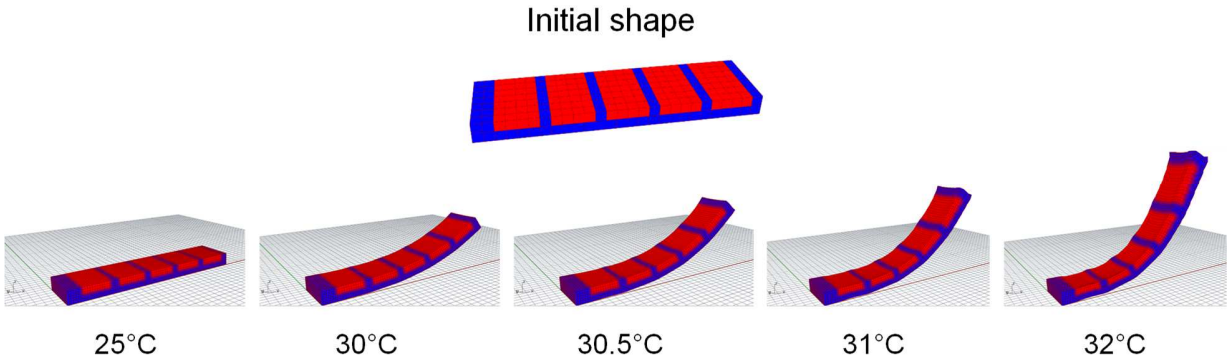

Fig. 9 - Hydrogel actuator

The hydrogel (red) sections do shrink in the three dimensions as expected and the generated eigenstrain clearly induces a bending motion. Nevertheless there is a discrepancy between the way the actuator bends in our model and theirs. In both models the actuator bends upwards. In our modeling scheme, as the temperature increases sections near the fixed end bends downwards (without a curvature change). This bending motion is progressively reversed as one moves away from that end. This downward bending could be explained as an accommodation to the fixed end. In order to ascertain the actual behavior the actuator should be printed.

5. Conclusions and future work

In this paper a contribution has been made to SMs modeling and simulation for conceptual design. A voxel-based modeling framework has been put forth to model and simulate the behavior of both conventional materials and (non-programmable) shape changing SMs (np-SCM). With this modeling framework, the possibility is given to designers to rapidly test a given distribution of SMs and check how it behaves upon exposure to stimulus before proceeding into detail design. Chunking matter into voxels was motivated by the need to pattern different materials within a geometry and in any spatial arrangement. Another rationale behind this approach is to give designers the ability to benefit the material complexity capability now affordable by AM.

In the modeling scheme, the main computation occurs not on the voxels themselves but on the underlying frame formed by beams connecting the voxels' centers. The resulting frame's nodes' DOFs are then used to compute a deformation map for each beam and, using skinning (a set of computer graphics techniques

for animating characters), the voxels are morphed. Simple models of SMs, in the form of internal forces changing the beams' lengths, have been introduced. These models are based on the actual behaviors of SMs including piezoelectric material, electro-/magneto-/photostrictive materials and hydrogel. The modeled materials are quite representative of this class of SMs. Furthermore, the methodology for deriving these materials' models can readily be used to derive models for others SMs.

A few simulations were run with the proposed modeling scheme in order to somehow validate it, both as regards conventional materials and SMs behaviors. The test cases used to gage the simulation engine include homogenous beam and plate, and heterogeneous beams (with materials of varying stiffnesses), as regards the conventional material behavior. For SMs, a printed smart hydrogel valve [36] and theoretical hydrogel actuators from [21] were simulated. All these simulation were quite fast and in pretty good agreement with either experiment or FEA. Worth highlighting nevertheless, is that the proposed voxel-based modeling and simulation scheme is not meant to be a surrogate to established methods such as FEM; rather it is a complimentary design tool mainly for conceptual design that precedes design efforts which can be invested in FEM. The goal is to rapidly specify any MD and check how it could behave.

In spite of the interesting results, our proposal still suffers from a number of limitations. The necessity to anchor at least one voxel hinders the simulation of free objects. Besides, the way stimuli, especially the scalar ones, are modeled typically ruled out the possibility to simulate deformations that could be induced by non-uniform stimuli fields. Finally in the current setting, voxels making up an object must be of the same size. An adaptive voxelization with a variable voxel size according to regions of interest could further reduce computation time and allow for bigger objects to be simulated.

In addition to the aforementioned limitations, future work can include effects such as collision, friction and gravity. Furthermore as regards materials, shape memory materials could also be modeled; the exploration of what a distribution including SMs of different types (e.g. one sensitive to heat and another sensitive to light) is another way of extending the modeling scheme.

From a practical perspective, a computational tool should embody the proposed modeling scheme (as initiated in [38]) while allowing for conventional CAD modeling capabilities. It should also let designers embrace the shape complexity capability peculiar to AM. Furthermore in addition to the given possibility of a seamless modeling and simulation of any MD (forward scheme), there should be – based on the modeling scheme – a methodology for distribution computation, using a source and a target shape (backward scheme). Such generated distribution could be a starting point for a finer design. These latter two future works are the subject of another publication by this group.

CRediT authorship contribution statement

Germain Sossou: Conceptualization, Methodology, Writing – Original Draft. Hadrien Belkebir: Software. Frédéric Demoly: Funding acquisition, Supervision, Conceptualization, Writing – Review & Editing. H. Jerry Qi: Writing – Review & Editing. Samuel Gomes, Ghislain Montavon: Supervision.

Acknowledgements

This research activity is part of much larger project in the field of design for 4D printing. The authors would like to thank the Ministère de l'Enseignement Supérieure et de la Recherche, the French

“Investissements d’Avenir” program, project ISITE-BFC (contract ANR-15-IDEX-0003) as main financial supports of this research program, and S.mart Franche-Comté network for their participation.

References

1. Hull, C.W., *Apparatus for production of three-dimensional objects by stereolithography*. 1986, Google Patents.
2. Vaezi, M., et al., *Multiple material additive manufacturing – Part 1: a review.* Virtual and Physical Prototyping, 2013. **8**(1): p. 19-50.
3. Stratasys. *PolyJet Technology for 3D Printing*. 03/21/2018]; Available from: http://www.stratasys.com/polyjet-technology.
4. Yamaguchi, K., et al., *Generation of three-dimensional micro structure using metal jet.* Precision Engineering, 2000. **24**(1): p. 2-8.
5. Tibbits, S., *4D Printing: Multi-Material Shape Change.* Architectural Design, 2014. **84**(1): p. 116-121.
6. Ferrara, M. and M. Bengisu, *Materials that Change Color*. PoliMI SpringerBriefs. 2014: Springer International Publishing. 139.
7. Hristoforou, E. and A. Ktena, *Magnetostriction and magnetostrictive materials for sensing applications.* Journal of Magnetism and Magnetic Materials, 2007. **316**(2): p. 372-378.
8. Peterson, G.I., et al., *3D-printed mechanochromic materials.* ACS Appl Mater Interfaces, 2015. **7**(1): p. 577-83.
9. Choi, J., et al., *4D Printing Technology: A Review.* 3d Printing and Additive Manufacturing, 2015. **2**(4): p. 159-167.
10. Leist, S.K. and J. Zhou, *Current status of 4D printing technology and the potential of light-reactive smart materials as 4D printable materials.* Virtual and Physical Prototyping, 2016: p. 1-14.
11. Khoo, Z.X., et al., *3D printing of smart materials: A review on recent progresses in 4D printing.* Virtual and Physical Prototyping, 2015. **10**(3): p. 103-122.
12. Momeni, F., et al., *A review of 4D printing.* Materials & Design, 2017. **122**: p. 42-79.
13. Mulakkal, M.C., et al., *Responsive cellulose-hydrogel composite ink for 4D printing.* Materials & Design, 2018. **160**: p. 108-118.
14. Baker, A.B., et al., *4D printing with robust thermoplastic polyurethane hydrogel-elastomer trilayers.* Materials & Design, 2019. **163**: p. 107544.
15. Thompson, M.K., et al., *Design for Additive Manufacturing: Trends, opportunities, considerations, and constraints.* CIRP Annals - Manufacturing Technology, 2016. **65**(2): p. 737-760.
16. Bodaghi, M., A.R. Damanpack, and W.H. Liao, *Adaptive metamaterials by functionally graded 4D printing.* Materials & Design, 2017. **135**: p. 26-36.
17. Bodaghi, M., A.R. Damanpack, and W.H. Liao, *Self-expanding/shrinking structures by 4D printing.* Smart Materials and Structures, 2016. **25**(10): p. 105034.
18. Bodaghi, M., A.R. Damanpack, and W.H. Liao, *Triple shape memory polymers by 4D printing.* Smart Materials and Structures, 2018. **27**(6): p. 065010.
19. Ge, Q., et al., *Multimaterial 4D Printing with Tailorable Shape Memory Polymers.* Sci Rep, 2016. **6**: p. 31110.
20. Noumenon. *The material is the mechanism*. 03/21/2018]; Available from: http://noumenon.eu/#&panel1-12.
21. Westbrook, K.K. and H.J. Qi, *Actuator Designs using Environmentally Responsive Hydrogels.* Journal of Intelligent Material Systems and Structures, 2008. **19**(5): p. 597-607.

22. Jacobson, A., et al., *Skinning: Real-time Shape Deformation*. ACM SIGGRAPH 2014 Courses. 2014.
23. Biswas, A., V. Shapiro, and I. Tsukanov, *Heterogeneous material modeling with distance fields.* Computer Aided Geometric Design, 2004. **21**(3): p. 215-242.
24. Gupta, V. and P. Tandon, *Heterogeneous object modeling with material convolution surfaces.* Computer-Aided Design, 2015. **62**: p. 236-247.
25. Okereke, M. and S. Keates, *Direct Stiffness Method*, in *Finite Element Applications: A Practical Guide to the FEM Process*. 2018, Springer International Publishing: Cham. p. 47-106.
26. Hjelmstad, K.D., *The Linear Theory of Beams*, in *Fundamentals of Structural Mechanics*. 2005, Springer US: Boston, MA. p. 241-291.
27. Lefebvre, E., et al. *Smart materials: development of new sensory experiences through stimuli responsive materials*. in *5th STS Italia Conference A Matter of Design: Making Society through Science and Technology*. 2014. Milan, Italy: STS Italia.
28. Pelrine, R.E., R.D. Kornbluh, and J.P. Joseph, *Electrostriction of polymer dielectrics with compliant electrodes as a means of actuation.* Sensors and Actuators A: Physical, 1998. **64**(1): p. 77-85.
29. Zhao, Q., H.J. Qi, and T. Xie, *Recent progress in shape memory polymer: New behavior, enabling materials, and mechanistic understanding.* Progress in Polymer Science, 2015. **49–50**: p. 79-120.
30. Mohd Jani, J., et al., *A review of shape memory alloy research, applications and opportunities.* Materials & Design, 2014. **56**: p. 1078-1113.
31. Ravichandran, G., *Active Materials*, in *Springer Handbook of Experimental Solid Mechanics*, N.W. Sharpe, Editor. 2008, Springer US: Boston, MA. p. 159-168.
32. Eyraud, L., et al., *Matériaux électrostrictifs pour actuateurs.* Revue de Physique Appliquee, 1988. **23**(5): p. 879-889.
33. Kundys, B., *Photostrictive materials.* Applied Physics Reviews, 2015. **2**(1): p. 011301.
34. Finkelmann, H., et al., *A new opto-mechanical effect in solids.* Phys Rev Lett, 2001. **87**(1): p. 015501.
35. Zhou, Y., et al., *Giant photostriction in organic-inorganic lead halide perovskites.* Nat Commun, 2016. **7**: p. 11193.
36. Bakarich, S.E., et al., *4D Printing with Mechanically Robust, Thermally Actuating Hydrogels.* Macromolecular Rapid Communications, 2015. **36**(12): p. 1211-1217.
37. Bakarich, S.E., et al., *Three-Dimensional Printing Fiber Reinforced Hydrogel Composites.* ACS Applied Materials & Interfaces, 2014. **6**(18): p. 15998-16006.
38. Sossou, G., et al., *Design for 4D printing: rapidly exploring the design space around smart materials.* Procedia CIRP, 2018. **70**: p. 120-125.

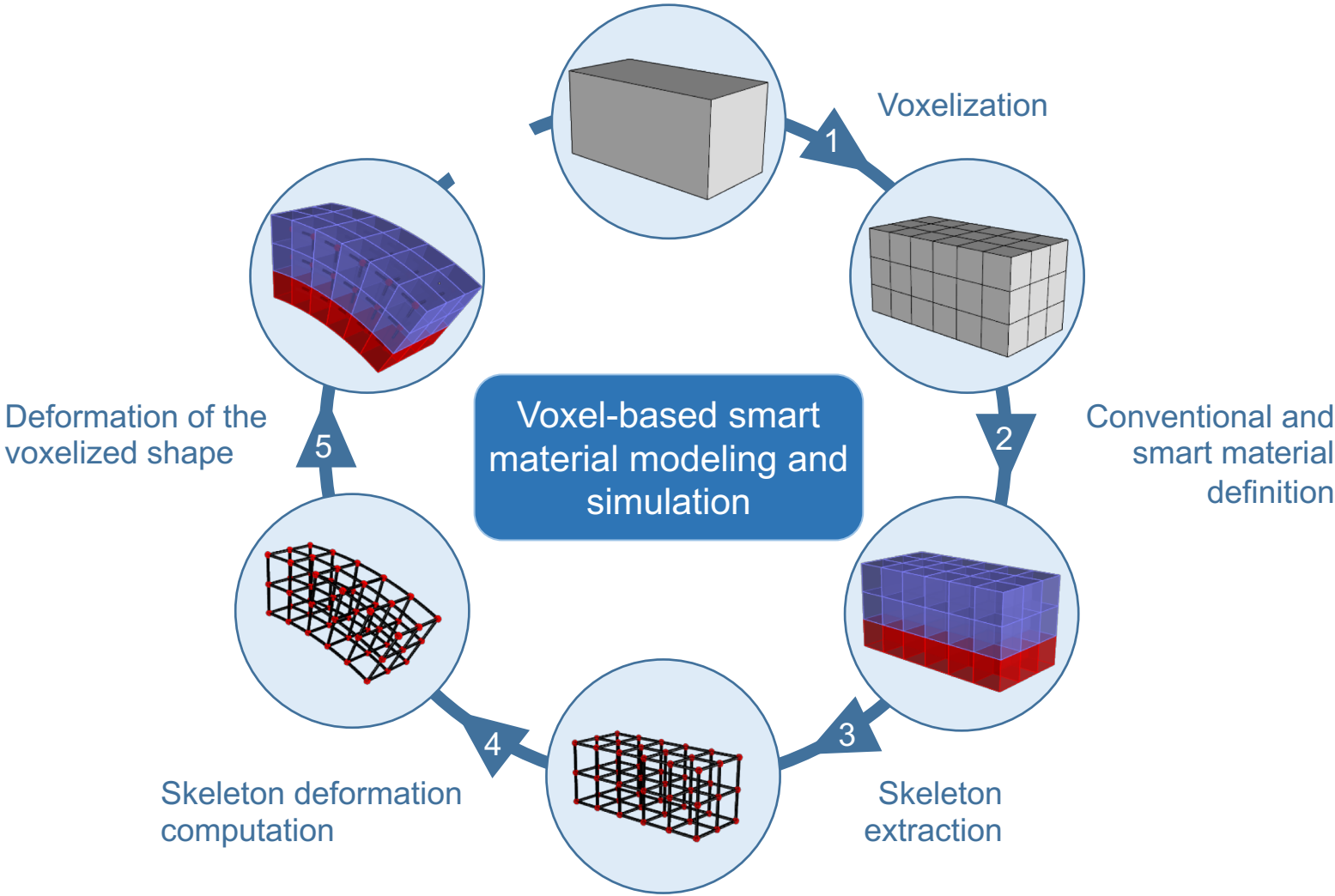
Voxel-based smart material modeling and simulation
1
Voxelization
2
Conventional and smart material definition
3
Skeleton extraction
4
Skeleton deformation computation
5
Deformation of the voxelized shape